Materials Advances

ROYAL SOCIETY OF CHEMISTRY

PAPER

View Article Online
View Journal | View Issue

Cite this: *Mater. Adv.*, 2025, **6**, 1621

Effect of bovine serum albumin (BSA) variants on the photophysical and biological properties of a NIR-responsive BSA–indocyanine green complex†

Jayashree Roy,[a] Devendra Tiwari,[a] Sahely Saha,[b] Raviraj Vankayala,[a] Shanmuga Sharan Rathnam Vuppaladadium,[c] Abhijeet Joshi[c] and Indranil Banerjee *[a]

In this study, we have investigated the effect of variants of BSA on the NIR-induced phototherapeutic performance of the BSA–ICG complex to identify the best BSA variant for complexing with ICG. Three variants of BSA, namely BSA-A7030 (protease, fatty acid, and globulin free), BSA-A3059 (protease & globulin free), and BSA-A3294 (only protease free), were chosen. UV-vis-NIR absorption, fluorescence, and CD spectroscopy studies showed no significant difference in the spectra of all the BSAs, but in the presence of Cu^{2+}, a differential reactivity of the three BSA variants was noticed. The biophysical study of the BSA–ICG complexes (1 : 1 molar ratio) showed that post-binding, there was a significant red shift of the ICG peak (both absorption and fluorescence) for BSA-A7030 with a widening of the excitation–emission hotspot. The photothermal properties of the BSA–ICG complexes under NIR (808 nm) exposure were similar to those of free ICG, whereas the photodynamic property increases for BSA-A3059. All the BSA–ICG complexes were found to be cytocompatible when tested with the NIH 3T3 cell line *in vitro*. The effect of the BSA type on the 808 nm NIR-mediated phototherapeutic properties of the BSA–ICG complex was tested *in vitro* on lung cancer cell line A549 (2D model) and a 3D osteosarcoma spheroid model. The study showed a NIR-induced cytoskeletal disruption of A549 cells with maximum damage caused by the BSA-A7030–ICG complex. The same complex was found to show the highest phototherapeutic effect on the 3D spheroid model. This study implied that an appropriate BSA variant is crucial for BSA–ICG complex-mediated NIR phototherapy.

Received 25th January 2025,
Accepted 3rd February 2025

DOI: 10.1039/d5ma00066a

rsc.li/materials-advances

1. Introduction

In recent years, near-infrared (NIR) responsive phototherapy has gained attention as a promising therapeutic modality for cancer.[1] In principle, the approach involves the use of a NIR absorbing material, which under the exposure of NIR of definite wavelength gets excited and subsequently produces heat (photothermal therapy, PTT) or reactive chemical species (photodynamic therapy, PDT) or both together.[2–4] One of the preferred materials for NIR responsive phototherapy is indocyanine green (ICG), which is a versatile amphiphilic tricarbocyanine dye known for its strong NIR absorption.[5] It has been experimentally proved that ICG confers therapeutic benefits by both PTT and PDT. The US Food and Drug Administration (FDA) has already approved the use of ICG in medical diagnosis and imaging.[5,6] Furthermore, since ICG also provides fluorescence upon NIR activation it is often used as a diagnostic and theranostic agent.[7]

However, free ICG showed some limitations when used in therapeutic formulations. The major drawbacks are its short plasma half-life and poor stability in aqueous systems.[8–10] To address this issue, Jiang *et al.* recently reported ICG-derived carbon dots that showed improved photothermal efficiency.[11] Interestingly, it was observed that ICG has an affinity to human serum albumin (HSA), and binding with albumin leads to chemical stability.[12,13] Such findings inspired scientists to develop the ICG–albumin complex to impart stability in ICG therapeutic formulations. In addition to HSA, bovine serum albumin (BSA) has also shown similar interaction with ICG because of its close homology with HSA.[14,15] Other advantages of BSA are its biocompatibility, less immunogenicity, ready availability, and low-cost.[16–18] As a result, BSA has often been used along with ICG to develop effective anticancer formulations. There are several examples available in the

[a] *Department of Bioscience and Bioengineering, Indian Institute of Technology Jodhpur, Karwar 342030, India. E-mail: indranil@iitj.ac.in*
[b] *Technology Innovation and Startup Center (TISC), Indian Institute of Technology Jodhpur, Karwar 342030, India*
[c] *Department of Biosciences and Biomedical Engineering, Indian Institute of Technology Indore, Khandwa Road, Indore 453552, Madhya Pradesh, India*

† Electronic supplementary information (ESI) available. See DOI: https://doi.org/10.1039/d5ma00066a

literature that describe the combination of BSA and ICG in different therapeutic or theranostic platforms. A novel phototheranostic nano complex for enhanced NIR fluorescence imaging has been reported by Feifei An *et al.*[14] This study revealed that the binding of ICG with albumin can enhance the stability and photoluminescence quantum yield (PLQY). Park *et al.* developed an ICG-based phototherapeutic platform using PEG-BSA-AgNP.[19] Rong Ma *et al.* synthesized BSA@ICG-DOX NPs. They demonstrated minimal toxicity, good photothermal properties, strong NIR fluorescence emission, and the potential to target cervical tumors.[20]

There are several varieties of BSA available in the market. A detailed list of online resources about different types of commercially available BSA is available in Table S1 (ESI†). Earlier reports suggest that the performance of BSA-based formulations can vary with different versions of BSA. Gamaliel Junren Ma *et al.* reported that defatted BSA which works better as an antifouling agent has conformation and absorption properties different than fatted BSA.[21] Regardless of the purification stage's fractionation method, BSA proteins that were devoid of fatty acids often performed better than those that were stabilized by fatty acids. Defatted BSA proteins showed less charge repulsion in the adsorbed state and lower conformational stability in the solution phase, which results in enhanced reactivity. Increased surface-induced denaturation and adsorption uptake provide better passivation coatings and more tightly packed adlayers. Yuhong Xiao *et al.* demonstrated that different BSA preparations used as blocking agents in an ELISA can lead to varying levels of non-specific binding.[22] To investigate if bovine C3 caused vaccinia virus complement control protein (VCP) binding, they tested several BSAs with rabbit anti-bovine C3 and goat anti-human C3b antibodies and found no signal, indicating the absence of bovine C3. Despite this, different BSA preparations, (globulin-free or low-endotoxin) are found to be capable of binding with VCP. This suggests that the process to create globulin-free, low endotoxin BSA (A2934) depletes it of a substance that binds to VCP, though the specific contaminant was not identified. In a separate study, it was shown by Rita Slaaby *et al.* that commercial and commonly used BSAs contain factors that influence the binding of BSA with IGF-I resulting in variation in the BSA concentration-dependent EC_{50} value up to 40-fold.[23] Since these studies imply that there are variations in BSA's preparations, they emphasized that mentioning the catalogue number of BSA is important to avoid such variability.

Now in the case of the BSA–ICG complex, despite widespread interest in developing suitable phototherapeutic platforms, it is not clear whether variation in the type of BSA has any impact on the properties (such as absorption, fluorescence, photothermal properties, and ROS generation) of the BSA–ICG complex and if yes, then what should be the preferred version of BSA. The reason for such a knowledge gap is that the majority of relevant research publications have only assessed one version of BSA without mentioning the type of BSA or the factors such as fatty acid, immunoglobulin, *etc.* present in it. The fact is that different commercial versions of BSA, even those made by the same company, have different methods for isolating the protein from bovine plasma. This point is frequently overlooked at the time of reporting the phototherapeutic effect of the BSA–ICG complex, which hinders the technical progress.

Keeping this perspective in mind, herein we have conducted a study to understand how the variation in BSA type affects the photophysical and biological properties of the BSA–ICG complex and what kind of BSA is a better partner for ICG for phototherapeutic applications. For this purpose, we have chosen three different types of BSA from Sigma Aldrich, namely, BSA fraction IV catalogue number (A7030, A3059, and A3294). The variation in physicochemical properties of all the BSAs was checked. Furthermore, the complexes formed between ICG and three different types of BSA were extensively studied with different biophysical techniques that include UV-vis-NIR absorption spectroscopy, CD spectroscopy, fluorimetry, *etc.* The photothermal and photodynamic properties of all three sets of BSA–ICG were also checked. Finally, the effect of these complexes on living cells was analyzed *in vitro* in a 2D and 3D spheroid model.

2. Materials and methods

2.1. Materials

Bovine serum albumin, heat shock fraction, protease free, fatty acid free, essentially globulin free, pH 7, ≥98% (Cat No. A7030), bovine serum albumin, heat shock fraction, protease free, essentially globulin free, pH 7, ≥98% (Cat No. A3059), bovine serum albumin, heat shock fraction, protease free, pH 7, ≥98% (Cat No. A3294), copper sulfate ($CuSO_4$, anhydrous powder, ≥99.99% trace metals basis, Cat No. 451657), 8-anilino-1-naphthalenesulfonic acid (ANS, Cat No. 10417), indocyanine green (ICG, Cat No. 21980), TRITC phalloidin (Cat No. P1951) and 2′,7′-diacetyldichlorofluorescein (DCFH-DA, Cat No. D6883) were purchased from Sigma Chemical Co. Dulbecco's modified Eagle's media (DMEM, Cat No. AL151A), Dulbecco's phosphate-buffered saline (DPBS, Cat No. TL006), fetal bovine serum (FBS, Cat No. RM10432), antibiotic–antimycotic solution (Cat No. A002A), 0.25% trypsin-1 mM ethylenediaminetetraacetic acid (EDTA, Cat No. T001) and MTT reagent (3-(4,5-dimethylthiazol-2-yl)-2,5-diphenyltetrazolium bromide, Cat No. CCK003) were purchased from Himedia, India. The NIH3T3, A549 and MG 63 cell lines were purchased from the National Centre for Cell Science, Pune.

2.2. Methodologies

2.2.1. Preparation of BSA stocks and other reagents. The BSA stock solutions (0.2 mM) of A7030, A3059, and A3294 were prepared in MilliQ water (18.2 MΩ). For the comparative analysis of important physicochemical properties of three types of BSAs, the aforementioned stock was further diluted in MilliQ water as per the experimental requirement. The ANS stock solution was prepared using Milli-Q water with a concentration of 3.16 mg mL^{-1} (10 mM). For the biophysical study of the interaction of different types of BSA with metal ions (Cu^{2+}), all BSA samples were prepared in MilliQ at 0.2 mM concentration. A 10 mM stock solution of copper sulfate was prepared in MilliQ and further diluted to 0.3 mM, 0.6 mM, and 0.9 mM in

MilliQ at the time of studying the interaction with different types of BSA. For the BSA–ICG complex formation, ICG stock (645 μM) was prepared in MilliQ water. For BSA–ICG complex formation, 500 μL of BSA (0.2 mM) and 155 μL of ICG (645 μM) were mixed and the volume was made up to 1 mL with MilliQ water. For cellular studies, BSA solution (0.2 mM) was prepared in incomplete media (DMEM). For every experiment, freshly prepared reagents were used.

2.2.2. UV-vis-NIR absorption spectroscopy. The absorption spectra of the three different BSA samples were measured using a Shimadzu UV-vis-NIR spectrophotometer (UV-1900i) from 200–1100 nm wavelength. For studying the interactions of different BSA with varying concentrations of Cu^{2+}, the absorption spectra were recorded for the 200–500 nm wavelength region. BSA–ICG sample spectra were recorded in the 200–900 nm wavelength region. For all the absorption spectra, ultrapure Milli-Q water was used as the blank as the samples were prepared in it. Quartz cuvettes having a 1 cm optical path length were used.

2.2.3. Fluorescence spectroscopy. The intrinsic fluorescence spectra of different BSAs were recorded using a Jasco spectrofluorometer (FP-8300) containing an Xe arc lamp (continuous output) as the excitation source. The slit widths for excitation and emission were kept at 2.5 nm. For intrinsic fluorescence measurements, all the samples with BSA were excited at 295 nm and the emission was collected from 300–500 nm wavelength. Spectra were recorded at 298 K with a 1 mL quartz cuvette of 1 cm optical path length. For this experiment, all the samples were diluted 10-fold with MilliQ to make up the volume to 1 mL. The spectra obtained through these experiments were analyzed using Origin software. For ICG fluorescence detection measurements, the sample was excited at 720 nm, and emission spectra were recorded at 735–900 nm.

For 3D excitation and emission mapping, the excitation wavelength range was 650–850 nm, and the emission wavelength range was 665–895 nm with a 10 nm increment. The excitation and emission bandwidth were set to 5 nm and 10 nm, respectively. Furthermore, the spectra were analyzed using Origin software. For 8-anilino-1-naphthalenesulfonic acid (ANS) fluorescence measurements, the fluorescence emission was recorded at the photoexcitation wavelength of 350 nm and the emission was collected from 400–600 nm wavelength. Before the fluorescence scan, the sample was incubated for 1 hour in the dark.

2.2.4. Circular dichroism (CD) spectroscopy. For secondary structure prediction of the different BSAs, CD measurements were done on a Jasco J 815 Spectropolarimeter, and the conformational changes of the BSA samples were monitored for the wavelength range 195–250 nm. For this experiment, 5 μM concentration of BSA was used. Samples were taken in a cuvette of 1 mm path length with a scanning speed of 50 nm min^{-1}.

2.2.5. Study of the NIR-induced photothermal effect. To study the photothermal properties of the BSA–ICG complex prepared with different types of BSA, samples were irradiated using an 808 nm CW laser at a power density of 0.33, 0.66, and 1 W cm^{-2} for 5 min, and the temperature rise was recorded using a thermal camera (Model No. FLIR Cx-series). Briefly, 300 μL of the sample was kept in a 1.5 mL microcentrifuge tube and was subjected to laser irradiation from the top keeping the lid of the microcentrifuge open. The temperature rise was recorded for 5 min at a 30 s time interval. MilliQ served as a control in this experiment. To study the photostability, the samples were irradiated with an 808 nm CW laser at a power density of 0.33 W cm^{-2} for 5 min, and allowed to cool down for 5 min with the laser off. Samples were exposed to the laser through five such on/off cycles to measure the temperature rise using a thermal camera (FLIR Cx-series). The cooling curve was obtained during the laser-off period.

2.2.6. Study of the NIR-induced photodynamic effect (analysis of acellular ROS generation). In the study of the NIR-induced ROS generation from different BSA–ICG complexes, the samples were analyzed through fluorimetry using DCFH-DA (a ROS probe) as per the protocol mentioned by Netra *et al.*[24] Briefly, sodium hydroxide (0.01 M) was mixed with DCFH-DA (200 μM) in a 3 : 2 v/v ratio and incubated for 30 min at room temperature to convert DCFH-DA to DCFH2. To stop the reaction, the mixture was poured into 0.1 M PBS (3 mL). DCFH2 was added to the BSA sample to obtain the final concentration of 5 μM. After that, the samples were subjected to 808 nm CW laser irradiation at a power density of 0.3 W cm^{-2} for 5 min. The resulting solution was excited at 405 nm and emission was recorded for the wavelength range spanning from 420–500 nm.

2.2.7. *In vitro* cytotoxicity assay. The *in vitro* cytotoxicity of the BSA–ICG complexes was evaluated by MTT assay using NIH3T3 mouse fibroblasts. The cells were cultured in complete DMEM, and incubated at 37 °C and 5% CO_2. For cytotoxicity studies, the cells were seeded in 96-well plates at a density of 10^4 cells per well and incubated overnight at 37 °C in an incubator (5% CO_2, 95% humidity).

The cells were then treated with 100 μL of BSA–ICG complex (0.1 mM) prepared in incomplete DMEM media and incubated for 4 h at 37 °C. The cells were then washed with PBS and treated with 100 μL of 0.5 mg mL^{-1} of MTT reagent and incubated for 3.5 h. Then, the MTT solution was removed and 100 μL of DMSO was added to each well to dissolve the formazan crystals, and the absorbance was measured at 570 nm using a microplate reader (Agilent EPOCH-SN). The experiment was done in triplicate. The statistical analysis was performed using one-way ANOVA for p-value < 0.05.

For the study of cytoskeletal reorganization, cells were cultured and treated with BSA–ICG complexes as per the method mentioned above. Post-treatment cells were fixed with 4% paraformaldehyde (in PBS), permeabilized with 0.1% Triton X, and then stained with TRITC (tetramethylrhodamine isothiocyanate) phalloidin and Hoechst. The cells were visualized through fluorescence microscopy (Olympus, USA).

2.2.8. Study of *in vitro* uptake of BSA–ICG complexes by A549 cells and cellular ROS generation. To compare the influence of different BSA on the uptake of the BSA–ICG complex by A549 lung cancer cells and subsequent generation of ROS under NIR exposure, 3×10^5 cells were seeded in 6 well plates for 48 h before treatment. The cells were then treated

with BSA–ICG complexes (0.1 mM, prepared in incomplete DMEM media) for 4 hours. Post incubation, the cells were trypsinized, washed with PBS, and resuspended in 500 μL of PBS. After that the cells were then irradiated with an 808 nm laser at a power density of 0.33 W cm^{-2} for 5 min. Post-irradiation cells were incubated for 30 minutes with DCFH-DA (a probe for ROS) washed two times with PBS to remove any remaining free DCFH-DA in the solution. Finally, the cells were resuspended in PBS and subjected to flow cytometry using a FACS BD Accuri C6 (BD Biosciences, San Jose, CA, USA). ROS signals were acquired at FL-1 (filter for FITC) and ICG signals in the cells were acquired at the APC-Cy7 channel (785 nm) filter as per the protocol reported.[25]

2.2.9. Study of the impact of NIR irradiation on the A549 cells treated with BSA–ICG complexes. To evaluate the effect of NIR irradiation on the A549 cells treated with different BSA–ICG complexes, 10^4 cells were seeded per well in 96-well plates and incubated overnight at 37 °C in an incubator (5% CO_2, 95% humidity). The cells were then treated with 100 μl of BSA–ICG complexes (0.1 mM) prepared in incomplete DMEM media and incubated for 4 h at 37 °C. The cells were then irradiated with an 808 nm CW laser at a power density of 0.33 W cm^{-2} for 5 min. Post irradiation, the cells were fixed with 4% paraformaldehyde (in PBS), permeabilized with 0.1% triton X, and then stained with TRITC (tetramethylrhodamine isothiocyanate) phalloidin and Hoechst. The cells were visualized through fluorescence microscopy (Olympus, USA).

2.2.10. Study of the NIR-mediated phototherapeutic effect of BSA–ICG formulations in a 3D spheroid model. To check the influence of BSA-types on the phototherapeutic effect of BSA–ICG complexes in a 3D tumors model, we prepared a cellular spheroid using the MG-63 cell line (osteosarcoma cell line).

To prepare spheroids, 60 μL of 0.6% agarose solution was poured into each well of a 96-well plate and allowed to solidify at room temperature for 10–15 min. A single-cell suspension containing 10^4 cells in complete DMEM medium was added to the solidified agarose bed in each well. The plate was incubated at 37 °C (in 5% CO_2, 95% humidity) for 4 days, allowing the cells to aggregate and form densely packed, spherical spheroids. Once the spheroids attained the spherical morphology, they were treated with BSA-A7030–ICG, BSA-A3059–ICG, and BSA-A3294–ICG complexes (0.1 mM) prepared in incomplete DMEM media and incubated for 4 h at 37 °C.

Following the incubation, the spheroids are exposed to 808 nm near-infrared (NIR) light at 1 W cm^{-2} for 10 min and then kept in an incubator for 4 hours. After this period, one set of spheroids was treated with 3 μM of propidium iodide (PI) and incubated for 20–30 min at 37 °C. The spheroids are subsequently washed three times with sterile 1× PBS. Finally, the spheroids are imaged using an Olympus IX73 inverted fluorescence microscope, capturing both phase contrast and fluorescence images to analyze spheroid integrity and PI uptake. Another set of spheroids (after treatment with BSA–ICG complex followed by NIR irradiation) was plated on a tissue culture plate and migration of the cells from the spheroid to the surface of the plate (analogues to explant culture) was checked after 96 h of plating. Post 96 h, images were captured using a phase contrast microscope. For quantitative analysis, following 4 hours of incubation all of the NIR light irradiation treatment groups were irradiated with an 808 nm laser for 10 min at a power density of 1 W cm^{-2} and then kept in an incubator for 3 hours. The cells were gently washed with 1× PBS, trypsinized, and neutralized in complete DMEM and were stained with 2 μM propidium iodide (PI) and incubated for 20–25 min at 37 °C. After that the cell population was analysed by flow cytometry to check the PI positive population.

3. Results & discussion

3.1. Comparative analysis of the biophysical properties of different BSAs (A7030, A3059 and A3294)

Analysis of the UV-vis absorption spectra of three different types of BSA in MilliQ is presented in Fig. 1A. We did not observe any significant variation in the absorption spectra of three different types of BSA. All the BSAs possessed two absorption peaks at 214 nm and 278 nm in MilliQ.[26,27] The spectrum shows a high absorption peak at 214 nm and a shoulder peak at 278 nm. The 214 nm absorption peak corresponds to the $\pi \rightarrow \pi$ transition, which is a characteristic of its backbone structure is C═O and the weak absorption peak at 278 nm is attributed to the presence of aromatic amino acids like tryptophan, tyrosine, and phenylalanine. The same findings were reported in other studies.[26,28] When checked for intrinsic fluorescence properties, and no variation in the spectral pattern was observed among the three BSAs, as shown in Fig. 1B. However, the peak intensity at 340 nm for BSA-A7030 was found to be relatively less in comparison to BSA-A3059 and BSA-A3294. It is already known that Trp fluorescence intensity often depends on the microenvironment of the protein.[29,30] Since BSA-A7030 has been reported as free of fatty acids and globulin, it can be inferred that the microenvironment of BSA-A7030 may be slightly different than the other two BSA types. Probing further with ANS revealed that there is a decrease in the ANS fluorescence for BSA-A7030 in comparison to the other two types of BSA (Fig. 1C). ANS as an extrinsic fluorophore gives a strong fluorescence signal in a hydrophobic environment.[31] A decrease in ANS fluorescence often happens because of the change in conformation of the protein that may lead to a more compact structure. Such changes can reduce the chances of binding of a smaller number of ANS molecules. Considering this finding along with the observation of intrinsic fluorescence study, it can be inferred that BSA without fatty acid and globulin allows maintaining its hydrophobic domain with lesser flexibility. However, when checked with CD spectroscopy, no significant change in the spectra was observed suggesting that the basic α-helical structure remains conserved irrespective of the presence or absence of fatty acid or globulin. The two negative bands at around 208 and 222 nm as observed in the CD spectra of all three variants of BSA, indicate the α-helical structure (Fig. 1D).[32] The negative ellipticity values of the three types of BSA at these wavelengths suggest no major

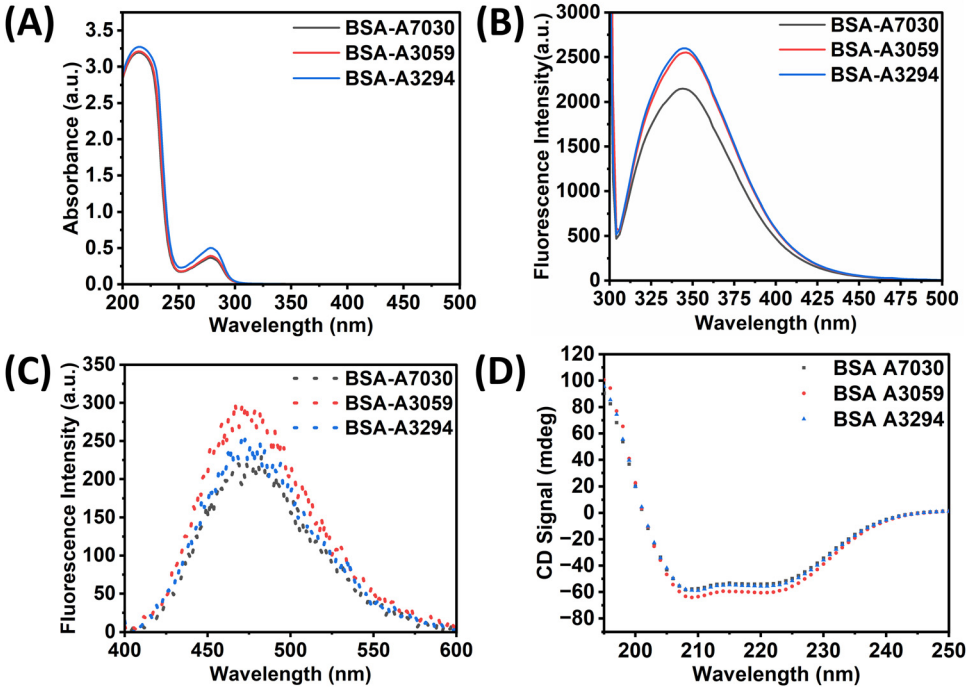

Fig. 1 Biophysical characterisation of all the BSAs (A) UV-vis absorption spectra. The spectra were taken for the range 200–1100 nm but reported for the range 200–500 nm since there were no features observed in the rest of the wavelength range; (B) intrinsic fluorescence emission spectra recorded at λ_{ex} = 295 nm and λ_{em} = 300–500 nm; (C) ANS fluorescence spectra recorded at λ_{ex} = 350 nm and λ_{em} = 400–600 nm; and (D) circular dichroism spectra in the far-UV region. All measurements were recorded in MilliQ water.

conformational changes in α-helical structure. Therefore, it can be assumed that the change in the microenvironment of Trp was the result of minor variations in the molecular arrangements around the two Trp residues.

3.2. Study of the interaction of different types of BSA with Cu(II) ions in aqueous medium

It is already known that albumin binds to d-block transition metal ions like Cu^{2+}, Zn^{2+}, *etc.* through its multiple binding sites, facilitating metal transport and regulation in the bloodstream.[33–36] We wanted to test the affinity of different types of BSA with these transition metal ions, so we decided to take Cu(II) as our model ion. To study the interaction of different BSA with Cu(II) at 37 °C temperature, for each type of BSA (0.1 mM), copper sulfate solutions of three different concentrations *i.e.* 0.3 mM, 0.6 mM, and 0.9 mM were used. Earlier, it was reported that BSA can form a visible precipitate when interacting with Cu^{2+} ions.[37] Here, we have observed that the formation of the copper-induced precipitation not only depends on the type of BSA, but also shows responsiveness towards the variation of Cu^{2+} concentration (Fig. 2D). We observed that the interaction of BSA-A7030 with Cu^{2+} (both at 0.6 mM and 0.9 mM) leads to the formation of a dense visible precipitate (high turbidity) whereas in the case of BSA-A3059 mild turbidity was observed even after interaction with Cu^{2+} ions at higher concentration *i.e.*, 0.9 mM. The other BSA *i.e.*, BSA-A3294 showed reactivity in between BSA-A7030 and BSA-A3059. Among all these sets we found maximum precipitation in the case of reaction between BSA-A7030 with Cu^{2+} (0.9 mM) whereas the least precipitation was observed for BSA-A3059 interacting with Cu^{2+} (0.3 mM). Earlier, it was reported that BSA can form a precipitate with Cu^{2+} when interacted in a 1 : 6 molar ratio.[37] It was also reported that such precipitation reaction was governed by Cu^{2+} and not by the anion or pH or temperature.

The Cu^{2+} concentration-dependent precipitation reactions with different BSAs were further monitored by UV-vis absorption spectroscopy and the spectra are reported in Fig. 2A–C. It was observed for all three BSAs that the characteristic UV peaks at 214 nm and 278 nm disappeared when treated with 0.9 mM of Cu^{2+}. Eventually, these are cases where visible precipitate formation was observed. In the case of interaction with 0.6 mM and 0.3 mM Cu^{2+}, it was observed that the peaks at 214 nm and 278 nm were retained for BSA-A3059 but not for the other two types of BSA. The binding of Cu(II) might induce partial unfolding or structural rearrangements in BSA, affecting the structure and thereby altering the absorbance characteristics.[38] To understand these phenomena in detail, the interaction was further studied by fluorescence spectroscopy and CD spectroscopy. The study of fluorescence quenching is a useful tool to get the structural information of the macro-molecule.[39] The intrinsic fluorescence spectra of all three BSAs with 0.6 mM Cu^{2+} were recorded (Fig. 2E). The samples were excited at 295 nm to specifically study the Trp fluorescence property.[40,41] It was observed that when Cu^{2+} was added into BSA, quenching of the 340 nm peak was least for BSA-A3059 whereas both BSA-A7030 and BSA-A3294 showed significant quenching. The UV and fluorescence data suggest that molecular structure BSA-A3059 remains unperturbed in the presence of Cu^{2+} whereas the other two BSAs are vulnerable to structural changes. This was

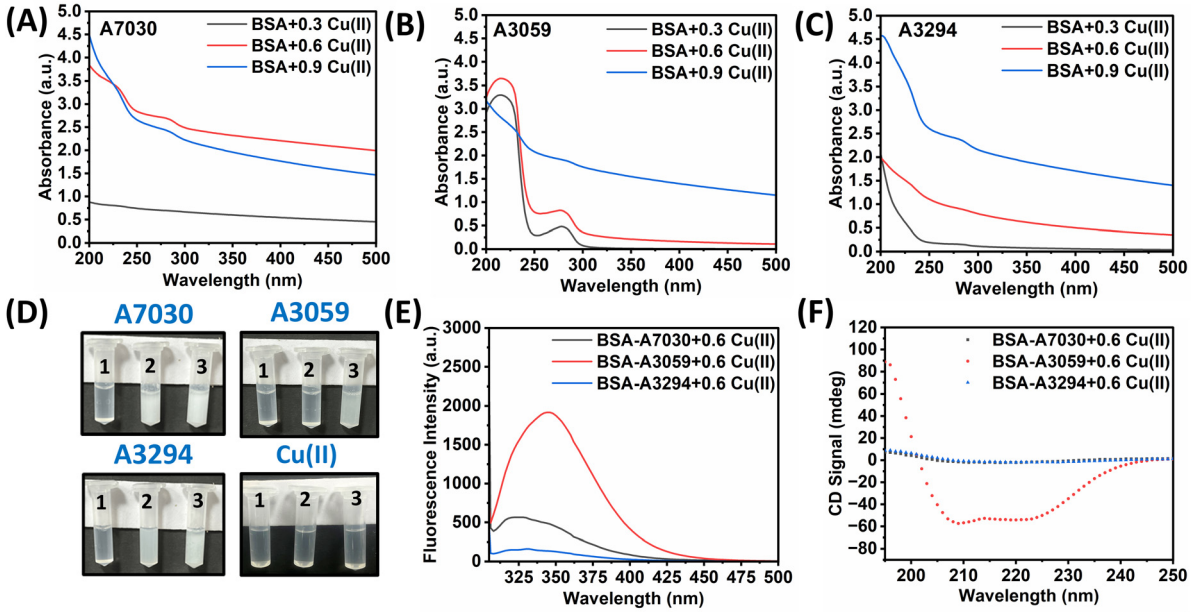

Fig. 2 Analysis of the interactions of BSA variants with Cu(II) ions: (A)–(C) UV-vis spectra from 200–500 nm of BSA-A7030, BSA-A3059, and BSA-A3294, respectively; (D) images showing the formation of Cu(II)-induced precipitation of BSA and Cu(II) solutions alone without BSA at 0.3 mM (1), 0.6 mM (2) and 0.9 mM (3), respectively; (E) and (F) interaction of BSAs with 0.6 mM Cu(II): (E) significant quenching observed in the intrinsic fluorescence spectra recorded at λ_{ex} = 295 nm and λ_{em} = 300–500 nm confirms complex formation; and (F) circular dichroism spectra in the far-UV region. All measurements were recorded in MilliQ water.

further proved by CD spectroscopy where characteristic CD spectra of BSA-A3059 were found unchanged indicating the retention of the native α-helical structure. The same was found completely lost in the case of BSA-A7030 and BSA-A3294 (Fig. 2F). These data together implied that three different BSAs can have different structures under the influence of metal ions.

3.3. Study of the interaction of different types of BSA with ICG in an aqueous medium

ICG is an FDA-approved near-infrared chromophore widely used in therapeutic applications for its exceptional tissue penetration capabilities.[7,42] ICG is crucial in phototherapy due to its strong absorption in the near-infrared range, which enhances photothermal and photodynamic therapeutic capabilities and facilitates effective targeting to mediate the destruction of cancer cells.[43,44] Free ICG poses several challenges in cancer treatment like poor circulation half-lives, rapid clearance, poor stability, and limited cellular uptake, *etc.*, while binding with BSA enhances its stability and half-life with a reduction in photodegradation.[45–49] Here, we have checked the binding of ICG with different types of BSA using a set of biophysical techniques.

The UV-vis-NIR absorption spectra of the three different BSAs and ICG are presented in Fig. 3A. It was found that the absorption peak intensities at 214 and 278 nm for BSA remained the same for all three types. However, in the NIR region, we observed a shift of the two characteristic ICG peaks, one from 710 nm to 728 nm (~18 nm) and another from 778 nm to 798 nm (~20 nm) when interacting with BSA-A3059 & BSA-A3294 with nominal change in the peak intensity. In the case of BSA-A7030, the red shift for the characteristic ICG peak was very significant, which is ~1.4 times higher for one peak from 710 nm to 735 nm (~25 nm) and ~3.5 times higher for

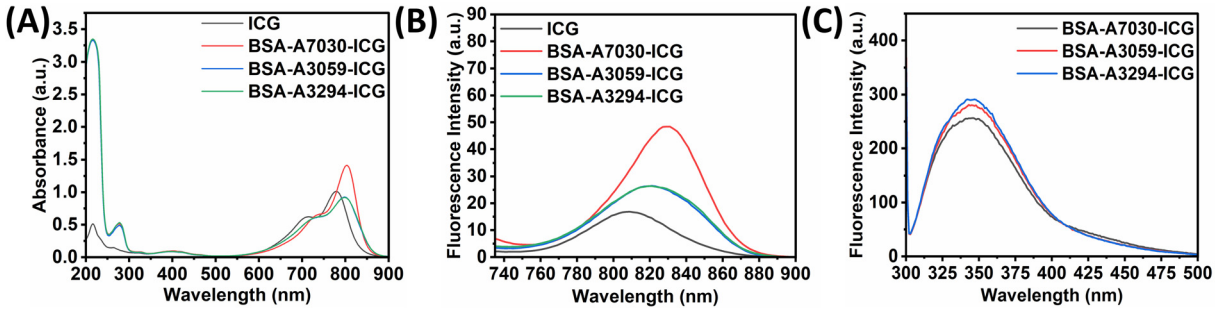

Fig. 3 Analysis of the interactions of BSA variants with ICG: (A) UV-vis-NIR spectra from 200–1100 nm show a red shift, which suggests complex formation; (B) fluorescence emission spectra with λ_{ex} = 720 nm and λ_{em} = 735–900 nm; and (C) intrinsic fluorescence spectra recorded at λ_{ex} = 295 nm and λ_{em} = 300–500 nm.

another peak from 728 to 803 nm (~75 nm), when compared to free ICG. Earlier it was reported that a red shift occurs when ICG binds with BSA.[50] However, here we have observed that the extent of redshift varies with the type of BSA, which implies differential binding of ICG with a different variant of BSA. When checked with other concentrations of BSA, we observed a concentration-dependent shift of characteristic ICG peaks, while no change was observed for the absorbance peak of BSA for all three BSA–ICG complexes. Furthermore, for BSA-A7030–ICG, a concentration-dependent increase in the intensity of the ICG peak was observed (Fig. S2, ESI†).

The free ICG showed peak maxima at 809 nm, while all the BSA–ICG showed a redshift (Fig. 3B). The highest redshift (~20 nm) was observed for BSA-A7030 whereas the same for BSA-A3059 and BSA-A3294 was 14 nm, respectively. This data is in accordance with the UV-vis absorption spectra, as shown in Fig. 3A. Interestingly, when compared to free ICG, BSA-A7030–ICG exhibited a fluorescence enhancement of ~3 fold, whereas BSA-A3059–ICG and BSA-A3294–ICG showed only ~1.7 fold. When tested with varying concentrations of BSA, a concentration-dependent red shift of the emission peak of ICG at higher concentration of BSA with an increase in intensity for BSA-A7030–ICG was noticed (Fig. S3, ESI†). A decrease in the intensity of the peaks at 340 nm (quenching) for all the cases implies the strong binding of ICG with different BSAs (Fig. 3C).

3.4. Study of BSA dependent variation in the excitation–emission map for BSA–ICG complexes

To determine the fluorescence characteristics of these formulations, we have recorded the excitation–emission (ExEm) maps for free ICG, and various BSA–ICG complexes (BSA-A7030, A3059 & A3294), and the data for the same are presented in Fig. 4(A–D). The ExEm mapping for free ICG showed the two distinct emission hotspots, 685–705 nm, and 795–810 nm, upon excitation windows of 670–680 nm and 768–785 nm, respectively. This finding is in accordance with the published literature.[51–53]

For all the BSA–ICG complexes, there are two distinct features observed in the ExEm maps. Firstly, we observed that the emission hotspot emission window in the region of 685–705 nm, which was prominent in the case of free ICG, becomes unnoticeable. Secondly, there is a broadening of emission hot spots with a significant increase in intensity. The maximum broadening of the hotspot and increase in intensity was observed in the case of the BSA-A7030–ICG complex followed by BSA-A3059 and BSA-A3294 (almost similar enhancement). For the BSA-A7030–ICG complex, the excitation wavelength ranges between 780–830 nm, and the emission ranges between 800–855 nm. Furthermore, in comparison to ICG, the intensity of the hotspot for the BSA-A7030–ICG complex was found to be ~2.5 fold higher. For the BSA-(A3059 & A3294)–ICG complex, the excitation wavelength ranges between 785–825 nm and the emission wavelength ranges between 804–846 nm. When checked with other concentrations of BSA, we observed a concentration-dependent broadening of the hot spot and the extent of such broadening was found to be the highest for BSA-A7030–ICG (Fig. S4, ESI†). The broader 3D fluorescence excitation–emission window for the BSA-A7030–ICG complex suggests that this can be excited by a wider range of wavelengths

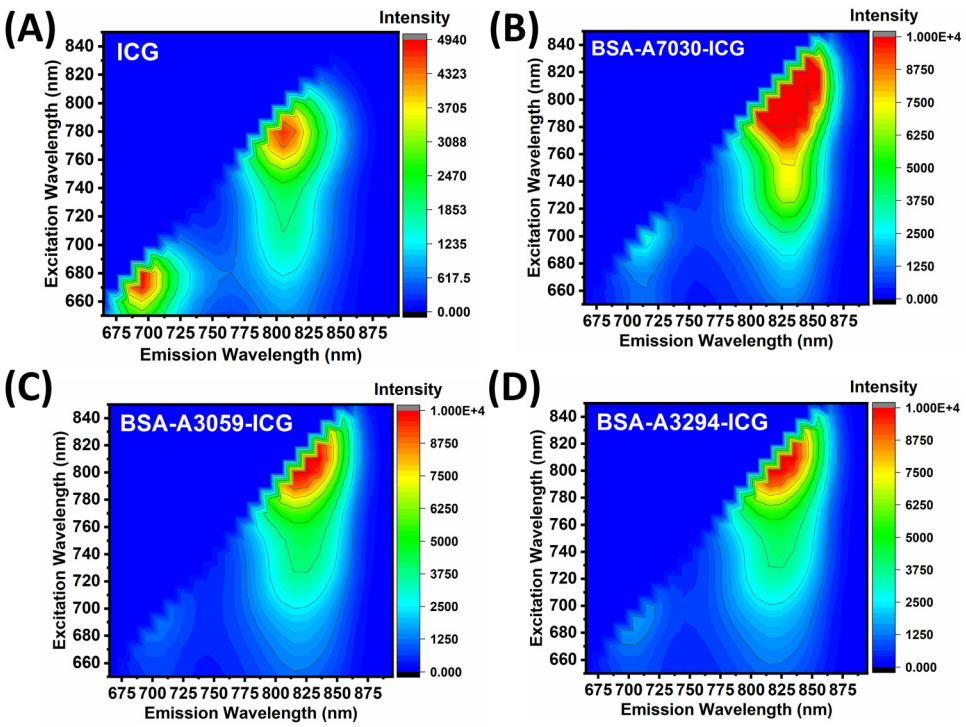

Fig. 4 Excitation–emission mapping of (A) ICG, (B) BSA-A7030–ICG, (C) BSA-A3059–ICG, and (D) BSA-A3294–ICG. All measurements were recorded in MilliQ.

and can emit at a wider wavelength suitable for better detection. This change in property makes BSA–ICG more versatile. These ExEm maps are universal and can be used to identify the brightest hotspot, at a given excitation wavelength.

3.5. Study of the NIR-induced photothermal and photodynamic properties of different BSA–ICG complexes in an acellular environment

When excited by an 808 nm NIR laser, ICG exhibits dual functionality. Upon activation, ICG sensitizes the production of singlet oxygen and other oxygen-centered radicals *via* a photodynamic process, while also absorbing NIR light to convert energy into heat through photothermal effects.[24,54] The photothermal properties of all the BSA–ICG complex formulations under the exposure of an 808 nm laser were investigated. At 0.3 W cm^{-2} NIR exposure, the change in the temperature (ΔT) for the BSA-A7030–ICG complex was found to be 23.6 °C. The same for 0.6 W cm^{-2} and 1 W cm^{-2} NIR exposure were found to be 38.3 °C and 57 °C, respectively. In the case of BSA-A3059, the changes in the temperature for 0.3 W cm^{-2}, 0.6 W cm^{-2}, and 1 W cm^{-2} were found to be 21.6 °C, 33.6 °C and 56.5 °C, respectively. For the BSA-A3294–ICG complex, the increase in temperature (ΔT) for 0.3 W cm^{-2}, 0.6 W cm^{-2}, and 1 W cm^{-2} was found to be 20.3 °C, 34.3 °C and 54.1 °C, respectively. The time-dependent variation of ΔT for all these BSA–ICG complexes under NIR exposure is presented in Fig. 5A–C. When compared with free ICG, we did not notice any significant enhancement in the photothermal properties of the BSA–ICG complexes. This suggests that for the particular NIR exposure (at 808 nm), all the BSA–ICG complexes exhibit similar photothermal effects at par with free ICG. When checked for the photothermal stability for 5 cycles (detail protocol mentioned in Section 2.2.4), we found that all the BSA–ICG complexes are equally photostable (Fig. 5D). The photostability of free ICG and photo images of the irradiated samples with all three BSA–ICG complexes and ICG are given in Fig. S5 (ESI†).

The photodynamic properties, *i.e.*, the capacity to generate ROS by different BSA–ICG complexes under NIR exposure, were further checked using DCFH-DA. The DCF fluorescence was found to be approximately 10-fold higher for free ICG when compared to the dark. The DCF fluorescence originating from the BSA-A3059–ICG, BSA-A3294–ICG, and BSA-A7030–ICG under photoirradiation conditions was 25 folds, 20 folds, and 17.5 folds higher respectively when compared to that of the dark condition (Fig. 5E). This could be attributed to the enhanced photostabilities of the BSA–ICG complexes when compared to free ICG.

3.6. *In vitro* cytotoxicity assay

ICG and BSA are both known for their high biocompatibility and are widely used in medical and biochemical applications.[46,47] However, the toxicity of the BSA–ICG complex was not evaluated in detail. Here the cytotoxicity of the complex BSA–ICG was determined by measuring the cell viability and morphology of NIH3T3 cells to understand the effect of different BSAs in the BSA–ICG complex (Fig. 6). MTT assay revealed that the BSA-A7030–ICG and BSA-A3059–ICG complexes are more cytocompatible than the control (TCP). Among the three BSA–ICG complexes, BSA-A7030 showed the highest cytocompatibility (1.14-fold) followed by the BSA-A3059–ICG complex (Fig. 5A). When checked for the cytoskeletal organization of the adhered NIH 3T3 cells post-treatment with the BSA–ICG complexes, we did not

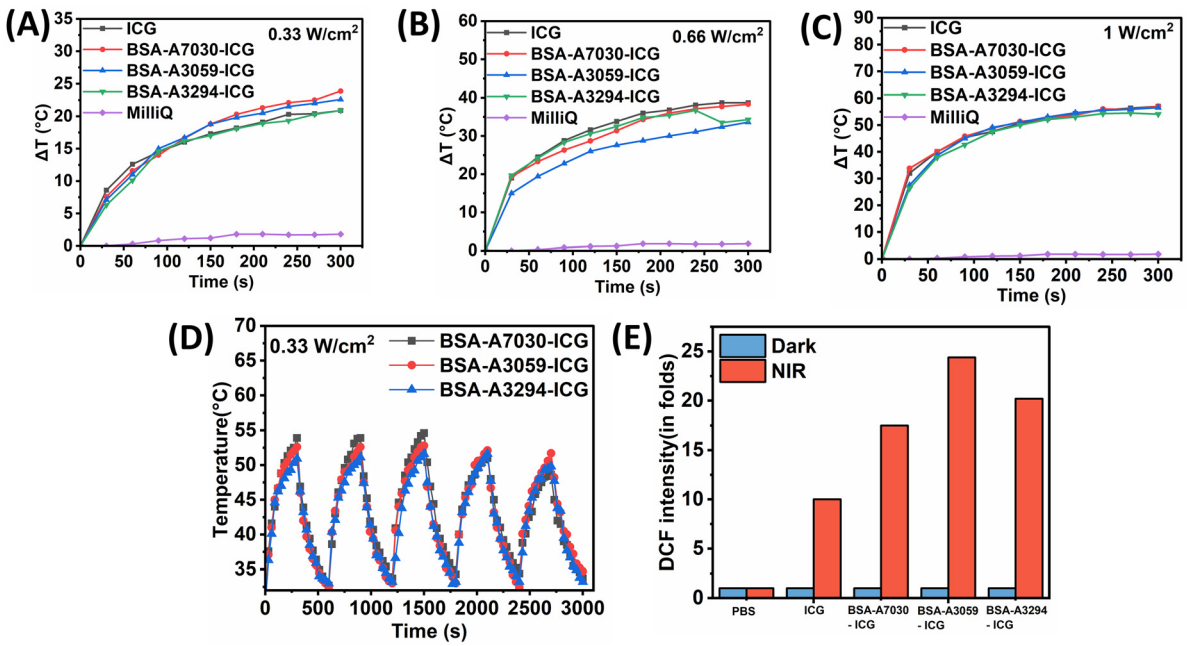

Fig. 5 (A)–(C) Photothermal temperature rise of ICG, BSA-A7030–ICG, BSA-A3059–ICG, and BSA-A3294–ICG with 0.33, 0.66 and 1 W cm^{-2}, respectively, when irradiated for 5 min; (D) photostability of BSA–ICG for five ON–OFF cycles; and (E) acellular ROS generation All measurements were recorded in deionized water.

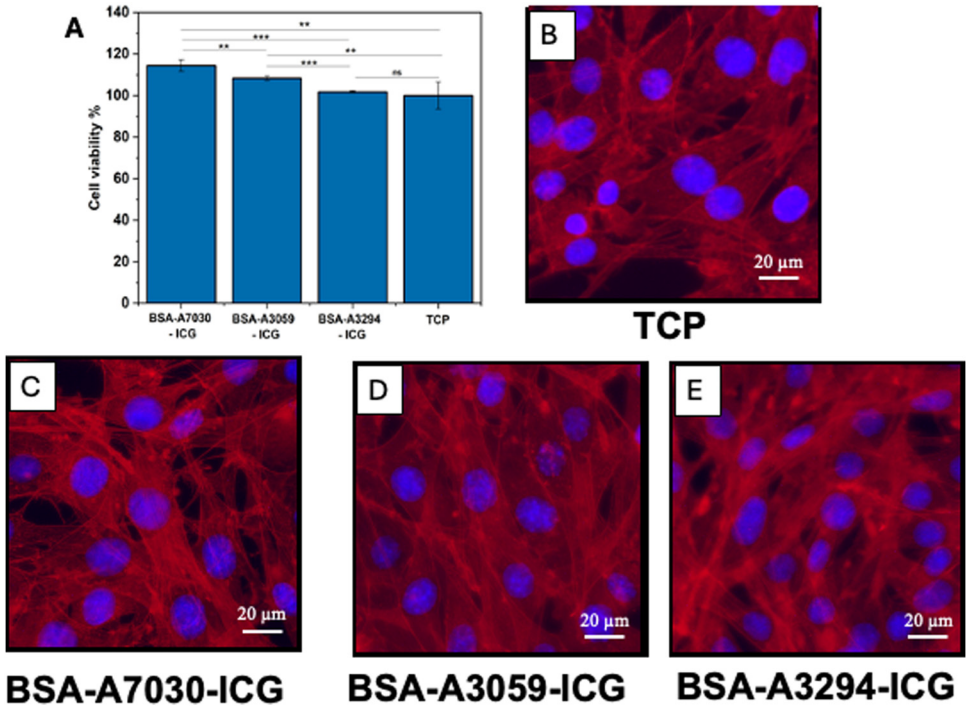

Fig. 6 (A) The cellular viabilities of NIH3T3 fibroblasts after exposure to BSA-A7030–ICG, BSA-A3059–ICG, BSA-A3294–ICG, and ICG measured by MTT assay. TCP was used as a control. The experiment was performed in triplicate and the data are presented as mean ± S.D. (*$p < 0.05$). Study of cytoskeletal organization of NIH 3T3 cells after treatment with (B) TCP, (C) BSA-A7030–ICG, (D) BSA-A3059–ICG, and (E) BSA-A3294–ICG (red colour – F-actin (TRITC phalloidin), blue colour – nucleus (Hoechst)).

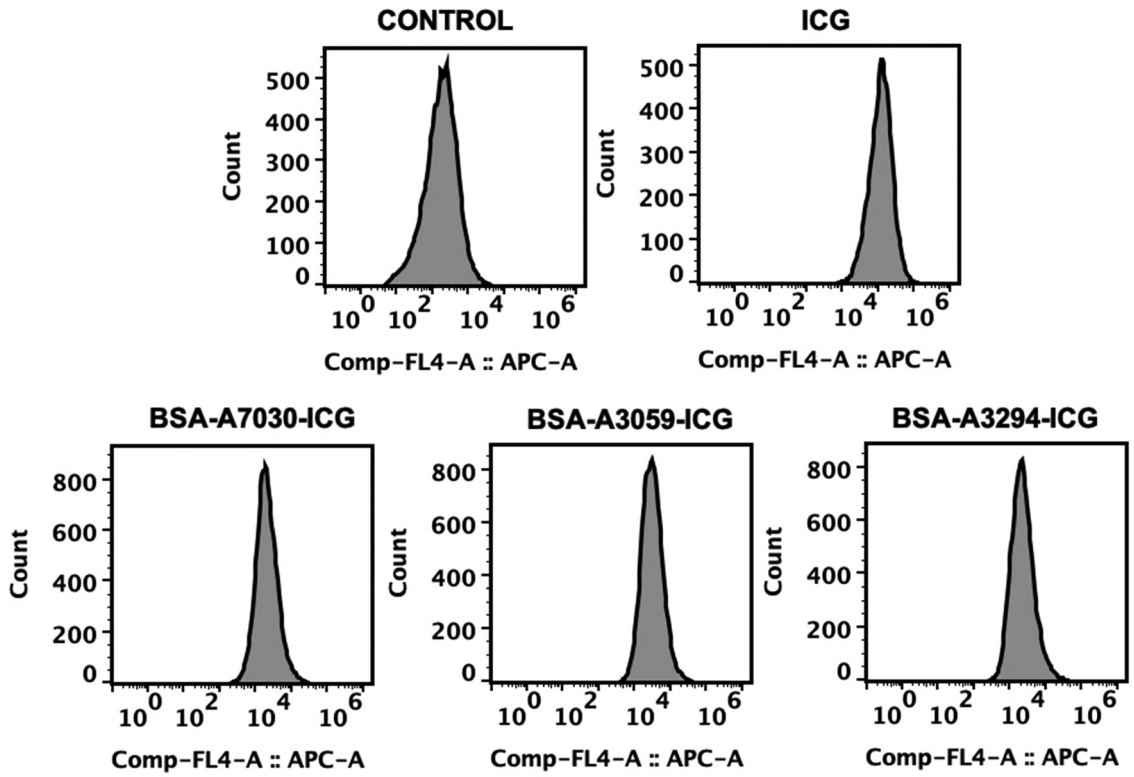

Fig. 7 Flow cytometry-based *in vitro* study of the uptake of ICG by A549 cells after treatment with the free ICG and BSA–ICG complex.

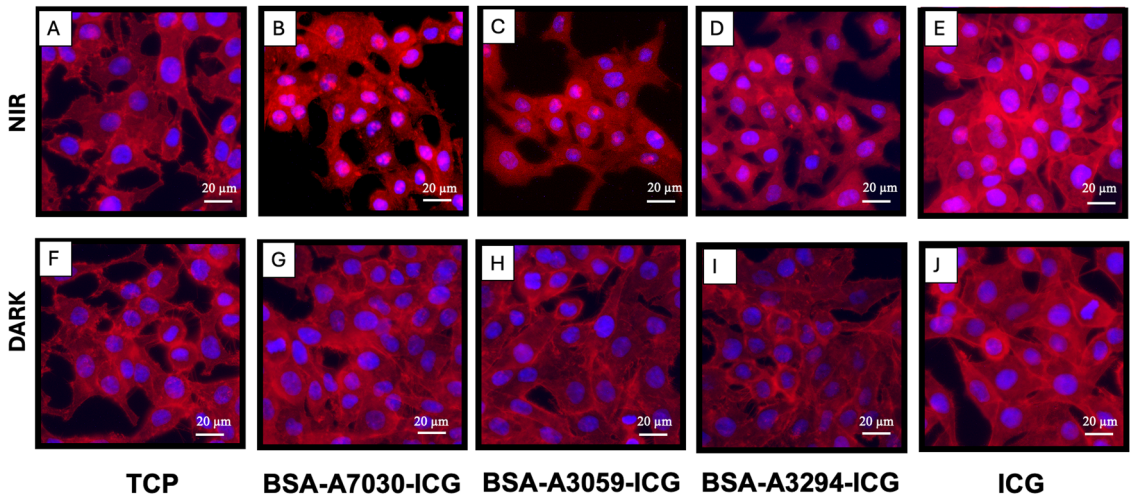

Fig. 8 A549 cells after treatment with BSA–CG complex for four hours. (A) and (F) TCP, (B) and (G) BSA-A7030–ICG, (C) and (H) BSA-A3059–ICG, (D) and (I) BSA-A3294–ICG, (E) and (J) ICG. (A)–(E) Fluorescent micrographs of cells after 808 nm NIR laser irradiation of 5 min at 0.33 W cm^{-2}, and (F)–(J) fluorescent micrographs of cells without NIR irradiation/dark conditions. Cells were stained with TRITC phalloidin (red) and Hoechst (blue).

observe any abnormalities in the F-actin distribution. All the cells were found to have characteristic morphology implying favorable adhesion.

3.7. Study of *in vitro* cellular uptake of BSA–ICG complexes by A549 cells

We were interested in understanding the influence of the type of BSA in the uptake of the BSA–ICG complex by the cells. To decipher this, we first treated the A549 cells with BSA–ICG complexes, and subsequently evaluated through flow cytometry to check the expression of ICG signals in the cell population. Earlier, it was reported by Wu, Menq-Rong *et al.* that ICG signals can be detected in flow cytometry by exciting ICG at the APC-Cy7 channel (785 nm) filter and detecting the signal using the following filter.[55] We observed that cells were able to take the BSA–ICG complexes and there was no distinct difference in the cellular signals for all the BSA–ICG complexes (Fig. 7). However, the peak cellular signals were slightly weak in comparison to free ICG. This could be because of the larger size of BSA–ICG complexes with respect to free ICG.

3.8. Study of the impact of NIR irradiation on the A549 cells treated with BSA–ICG complexes

ICG is a common reagent in NIR-induced phototherapy. It has already been reported that cells treated with ICG die under NIR exposure to photothermal and photodynamic effects. The

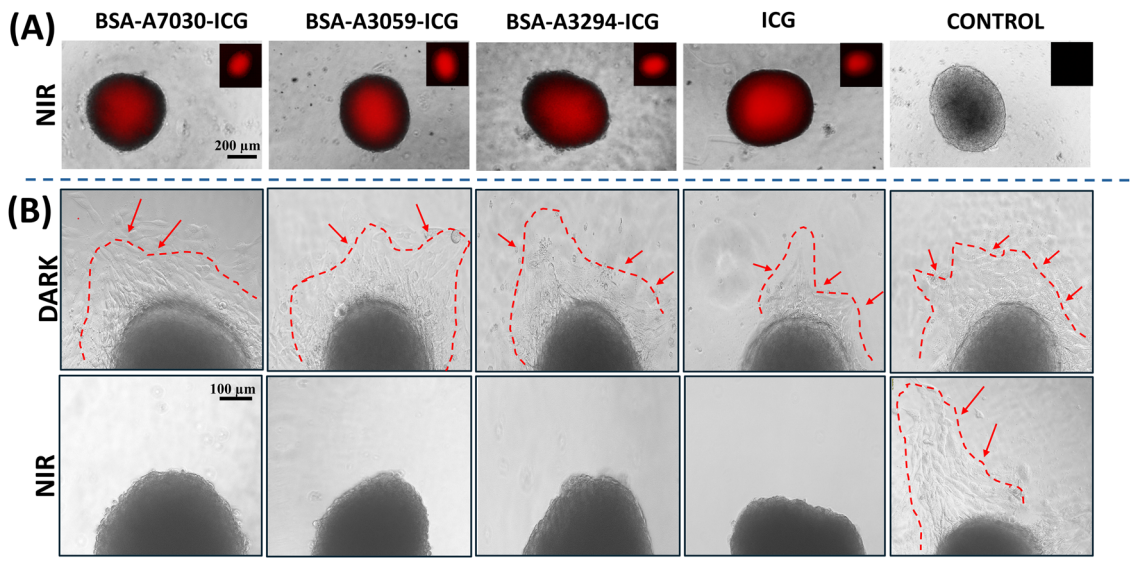

Fig. 9 Study of the *in vitro* therapeutic effect of the complexes in a 3D osteosarcoma spheroid model. (A) Fluorescence microscopic images of 4-day spheroids after PI staining; and (B) microscopic images of day 7 spheroids after 4 h of treatment under light and dark conditions: (i) BSA-A7030–ICG, (ii) BSA-A3059–ICG, (iii) BSA-A3294–ICG, (iv) ICG, and (v) control.

NIR-mediated phototherapy using ICG leads to cell death by both apoptotic and necrotic pathways with prominent disruption in the cytoskeleton[56,57] Here, we observed that there is a massive disruption of actin cytoskeleton post-NIR exposure for the cells treated with the BSA–ICG complex, which was not visible in the case of only NIR under the experimental conditions (Fig. 8). Furthermore, this effect was more visible in the BSA-A7030–ICG complex. This is to mention that without NIR irradiation (dark), no such cytoskeletal disruption was observed.

3.9. Study of the NIR-mediated phototherapeutic effect of the BSA–ICG formulation in a 3D bone tumor spheroid model

Because of the lack of similarities with native tissue organization, 2D *in vitro* models have limited acceptability in cancer research. A better option in this regard is the spheroid model.[58] So, far in the literature, many reports have tested the NIR formulation in the 3D spheroid model to gain insight into spheroids' death caused by nanoparticle photothermal disruption properties.[59,60] Here, to compare the effect of the type of BSA on the phototherapeutic effect of BSA–ICG complexes, we perform the experiment in a MG-63 spheroid model. A qualitative analysis revealed that treatment of spheroids with all three BSA–ICG complexes followed by NIR irradiation resulted in the uptake of PI, which implies cell death (Fig. 9A). However, without NIR exposure such an effect was not observed (data not shown). When the BSA–ICG treated and NIR irradiated cell spheroids are plated, we did not observe any cell migration from the spheroid to plate-surface (Fig. 9B, lower panel). However, in the case of the control, *i.e.* spheroids without (BSA–ICG treatment but with NIR exposure) and spheroids treated with BSA–ICG but without NIR exposure, a clear sign of cellular movement from spheroid to plate was observed (Fig. 9B, upper panel). When checked, quantitatively through flow cytometry (Fig. S6, ESI†), we found that BSA-A7030–ICG and BSA-A3294–ICG lead to 13% higher killing of cells in spheroids with respect to free ICG, whereas the same for BSA-A3059–ICG was almost similar to free ICG. This set of experiments clearly suggested that all three BSA–ICG complexes are capable of exerting cellular damage by NIR-induced phototherapeutic effect in the MG-63 spheroid model however their phototherapeutic effect varies with the type of BSA.

4. Conclusion

ICG is a well-explored molecule for NIR-responsive diagnostics and phototherapy. Since the photostability of ICG is relatively poor, it has often been complexed with serum albumin, which was found to be an effective strategy to overcome the aforesaid limitation of ICG. In this study, we showed that different variants of commercially available BSA can alter not only the excitation–emission properties of ICG but its photothermal and photodynamic properties as well. Our study showed that by choosing the appropriate variant of BSA, it is possible to increase the intensity and widen the wavelength range of the excitation–emission hot spot. This is important from the perspective of using different NIR wavelengths for phototherapy or diagnostics. Our study also showed that the selection of appropriate variants can significantly enhance the NIR-induced ROS generation (photodynamic effect) by ICG, which can make ICG more versatile and efficient. This was further proved *in vitro* against cancer cells. This understanding is important for developing BSA–ICG-based phototherapeutic formulations. So far, we have tested the different variants of the heat shock fraction of BSA. This is the first report that provides insight about the effect of the type of BSA on the photophysical properties of ICG. We also highlighted that the use of a specific type of BSA (BSA-A7030, which is fatty acid, globulin and protease free) can effectively widen the excitation–emission window and therefore enhance its prospects in phototherapeutic applications. It is quite possible that other types of BSA variants can provide even more encouraging results.

Author contributions

Indranil Banerjee: conceptualization, supervision, writing – original draft. Jayashree Roy: formal analysis, investigation, writing – original draft. Devendra Tiwari: investigation. Sahely Saha: investigation. V Shanmuga Sharan Rathnam: investigation. Raviraj Vankayala: review & editing. Abhijeet Joshi: methodology.

Data availability

The authors confirm that the data supporting the findings of this study are available within the article and its ESI.†

Conflicts of interest

There are no conflicts to declare.

Acknowledgements

The author would like to acknowledge the [i] fluorescence imaging facility created through the grant received from SERB (S/SERB/INB/20210079), [ii] facilities at the Duchenne Muscular Dystrophy (DMD) Research Centre at IIT Jodhpur, created through the IRPHA research grant scheme (IPA/2020/000015) funded by DST, SERB, and [iii] the Centre for Research and Development of Scientific Instrumentation (CRDSI) Facility at the Indian Institute of Technology Jodhpur and MoE, Government of India for the financial support to the author J. Roy & D. Tiwari.

References

1 B. Liu, C. Li, Z. Cheng, Z. Hou, S. Huang and J. Lin, Functional nanomaterials for near-infrared-triggered cancer therapy, *Biomater. Sci.*, 2016, **4**, 890–909.
2 K. F. Chu and D. E. Dupuy, Thermal ablation of tumours: biological mechanisms and advances in therapy, *Nat. Rev. Cancer*, 2014, **14**, 199–208.
3 J. P. Celli, B. Q. Spring, I. Rizvi, C. L. Evans, K. S. Samkoe, S. Verma, B. W. Pogue and T. Hasan, Imaging and

photodynamic therapy: Mechanisms, monitoring, and optimization, *Chem. Rev.*, 2010, **110**, 2795–2838.
4 D. E. J. G. J. Dolmans, D. Fukumura and R. K. Jain, Photodynamic therapy for cancer, *Nat. Rev. Cancer*, 2003, **3**, 380–387.
5 C. Shirata, J. Kaneko, Y. Inagaki, T. Kokudo, M. Sato, S. Kiritani, N. Akamatsu, J. Arita, Y. Sakamoto, K. Hasegawa and N. Kokudo, Near-infrared photothermal/photodynamic therapy with indocyanine green induces apoptosis of hepatocellular carcinoma cells through oxidative stress, *Sci. Rep.*, 2017, **7**, 1–8.
6 H. Wang, X. Li, B. W. C. Tse, H. Yang, C. A. Thorling, Y. Liu, M. Touraud, J. B. Chouane, X. Liu, M. S. Roberts and X. Liang, Indocyanine green-incorporating nanoparticles for cancer theranostics, *Theranostics*, 2018, **8**, 1227–1242.
7 A. Kumari, K. Kumari and S. Gupta, The effect of nanoencapsulation of ICG on two-photon bioimaging, *RSC Adv.*, 2019, **9**, 18703–18712.
8 V. Saxena, M. Sadoqi and J. Shao, Degradation Kinetics of Indocyanine Green in Aqueous Solution, *J. Pharm. Sci.*, 2003, **92**, 2090–2097.
9 A.-K. Kirchherr, A. Briel and K. Mäder, Stabilization of Indocyanine Green by Encapsulation within Micellar Systems, *Mol. Pharmaceutics*, 2009, **6**, 480–491.
10 C. D. Geddes, H. Cao and J. R. Lakowicz, Enhanced photostability of ICG in close proximity to gold colloids, *Spectrochim. Acta, Part A*, 2003, **59**, 2611–2617.
11 Y. Jiang, Z. Tan, T. Zhao, J. Wu, Y. Li, Y. Jia and Z. Peng, Indocyanine green derived carbon dots with significantly enhanced properties for efficient photothermal therapy, *Nanoscale*, 2023, **15**, 1925–1936.
12 W. Holzer, M. Mauerer, A. Penzkofer, R. M. Szeimies, C. Abels, M. Landthaler and W. Bäumler, Photostability and thermal stability of indocyanine green, *J. Photochem. Photobiol., B*, 1998, **47**, 155–164.
13 S. Chen, G. Yu, B. Zhang, Y. Wang, N. Zhang and Y. Chen, Human serum albumin (HSA) coated liposomal indocyanine green for in vivo tumor imaging, *RSC Adv.*, 2016, **6**, 15220–15225.
14 F. An, Z. Yang, M. Zheng, T. Mei, G. Deng, P. Guo, Y. Li and R. Sheng, Rationally assembled albumin/indocyanine green nanocomplex for enhanced tumor imaging to guide photothermal therapy, *J. Nanobiotechnol.*, 2020, **18**, 49.
15 N. Jiang, Z. Zhou, W. Xiong, J. Chen, J. Shen, R. Li and R. Ye, Tumor microenvironment triggered local oxygen generation and photosensitizer release from manganese dioxide mineralized albumin-ICG nanocomplex to amplify photodynamic immunotherapy efficacy, *Chin. Chem. Lett.*, 2021, **32**, 3948–3953.
16 J. Wang and B. Zhang, Bovine Serum Albumin as a Versatile Platform for Cancer Imaging and Therapy, *Curr. Med. Chem.*, 2017, **25**, 2938–2953.
17 S. Gao, G. Wei, S. Zhang, B. Zheng, J. Xu, G. Chen, M. Li, S. Song, W. Fu, Z. Xiao and W. Lu, Albumin tailoring fluorescence and photothermal conversion effect of near-infrared-II fluorophore with aggregation-induced emission characteristics, *Nat. Commun.*, 2019, **10**, 2206.
18 F.-F. An and X.-H. Zhang, Strategies for Preparing Albumin-based Nanoparticles for Multifunctional Bioimaging and Drug Delivery, *Theranostics*, 2017, **7**, 3667–3689.
19 T. Park, S. Lee, R. Amatya, H. Cheong, C. Moon, H. D. Kwak, K. A. Min and M. C. Shin, ICG-Loaded PEGylated BSA-Silver Nanoparticles for Effective Photothermal Cancer Therapy, *Int. J. Nanomed.*, 2020, **15**, 5459–5471.
20 R. Ma, N. Alifu, Z. Du, S. Chen, Y. Heng, J. Wang, L. Zhu, C. Ma and X. Zhang, Indocyanine green-based theranostic nanoplatform for nir fluorescence image-guided chemo/photothermal therapy of cervical cancer, *Int. J. Nanomed.*, 2021, **16**, 4847–4861.
21 G. J. Ma, A. R. Ferhan, J. A. Jackman and N. J. Cho, Conformational flexibility of fatty acid-free bovine serum albumin proteins enables superior antifouling coatings, *Commun. Mater.*, 2020, **1**, 1–11.
22 Y. Xiao and S. N. Isaacs, Enzyme-linked immunosorbent assay (ELISA) and blocking with bovine serum albumin (BSA)—not all BSAs are alike, *J. Immunol. Methods*, 2012, **384**, 148–151.
23 R. Slaaby, A. S. Andersen and J. Brandt, IGF-I binding to the IGF-I receptor is affected by contaminants in commercial BSA: the contaminants are proteins with IGF-I binding properties, *Growth Horm. IGF Res.*, 2008, **18**, 267–274.
24 Y. Prince, N. Hiremath and R. Vankayala, Near-infrared light activatable niosomes loaded with indocyanine green and plasmonic gold nanorods for theranostic applications, *Biomater. Sci.*, 2023, **11**, 7759–7767.
25 M.-R. Wu, Y.-Y. Huang and J.-K. Hsiao, Use of Indocyanine Green (ICG), a Medical Near Infrared Dye, for Enhanced Fluorescent Imaging—Comparison of Organic Anion Transporting Polypeptide 1B3 (OATP1B3) and Sodium-Taurocholate Cotransporting Polypeptide (NTCP) Reporter Genes, *Molecules*, 2019, **24**, 2295.
26 Y. Q. Wang, H. M. Zhang, G. C. Zhang, W. H. Tao, Z. H. Fei and Z. T. Liu, Spectroscopic studies on the interaction between silicotungstic acid and bovine serum albumin, *J. Pharm. Biomed. Anal.*, 2007, **43**, 1869–1875.
27 B. Lemli, D. Derdák, P. Laczay, D. Kovács and S. Kunsági-Máté, Noncovalent Interaction of Tilmicosin with Bovine Serum Albumin, *Molecules*, 2018, **23**, 1915.
28 D. Lu, X. Zhao, Y. Zhao, B. Zhang, B. Zhang, M. Geng and R. Liu, Binding of Sudan II and Sudan IV to bovine serum albumin: Comparison studies, *Food Chem. Toxicol.*, 2011, **49**, 3158–3164.
29 S. Cao, B. Liu, Z. Li and B. Chong, A fluorescence spectroscopic study of the interaction between Glipizide and bovine serum albumin and its analytical application, *J. Lumin.*, 2014, **145**, 94–99.
30 G. Li, B. S. Liu, Q. Zhang and R. Han, Investigation on the effect of fluorescence quenching of bovine serum albumin by cefoxitin sodium using fluorescence spectroscopy and synchronous fluorescence spectroscopy, *Luminescence*, 2016, **31**, 1054–1062.
31 P. Sen, M. M. Khan, A. Equbal, E. Ahmad and R. H. Khan, At very low concentrations known chaotropes act as

kosmotropes for the N and B isoforms of human serum albumin, *Biochem. Cell Biol.*, 2013, **91**, 72–78.

32 S. Biochemistry Lapanje, C. Tanford, R. H. Mcmenamy, Y. Lee, W. E. Moore, J. F. Foster, Y. Nozaki, M. Sogami, J. F. M. Foster, A. Petersen, K. Kawahara, S. Lapanje and K. P. Wong, Computed Circular Dichroism Spectra for the Evaluation of Protein Conformation, *Biochemistry*, 1969, **8**, 4108–4116.

33 W. Bal, J. Christodoulou, P. J. Sadler and A. Tucker, Multi-metal binding site of serum albumin, *J. Inorg. Biochem.*, 1998, **70**, 33–39.

34 W. Bal, M. Sokołowska, E. Kurowska and P. Faller, Binding of transition metal ions to albumin: Sites, affinities and rates, *Biochim. Biophys. Acta, Gen. Subj.*, 2013, **1830**, 5444–5455.

35 J. Bai, X. Sun, B. Geng and X. Ma, Interaction mechanism of Cu^{+}/Cu^{2+} on bovine serum albumin: Vitro simulation experiments by spectroscopic methods, *Spectrochim. Acta, Part A*, 2023, **293**, 122491.

36 P. P. Jing, Y. X. Li, Y. H. Su, W. L. Liang and Y. X. Leng, The role of metal ions in the behavior of bovine serum albumin molecules under physiological environment, *Spectrochim. Acta, Part A*, 2022, **267**, 120604.

37 V. E. Lee, J. M. Schulman, E. I. Stiefel and C. C. Lee, Reversible precipitation of bovine serum albumin by metal ions and synthesis, structure and reactivity of new tetrathiometallate chelating agents, *J. Inorg. Biochem.*, 2007, **101**, 1707–1718.

38 G. Navarra, A. Tinti, M. Leone, V. Militello and A. Torreggiani, Influence of metal ions on thermal aggregation of bovine serum albumin: Aggregation kinetics and structural changes, *J. Inorg. Biochem.*, 2009, **103**, 1729–1738.

39 J. Mariam, P. M. Dongre and D. C. Kothari, Study of Interaction of Silver Nanoparticles with Bovine Serum Albumin Using Fluorescence Spectroscopy, *J. Fluoresc.*, 2011, **21**, 2193–2199.

40 R. Starosta, F. C. Santos and R. F. M. de Almeida, Human and bovine serum albumin time-resolved fluorescence: Tryptophan and tyrosine contributions, effect of DMSO and rotational diffusion, *J. Mol. Struct.*, 2020, **1221**, 128805.

41 J. R. Lakowicz, *Principles of Fluorescence Spectroscopy*, Springer, US, Boston, MA, 1999, pp. 25–61.

42 K. Gowsalya, V. Yasothamani and R. Vivek, Emerging indocyanine green-integrated nanocarriers for multimodal cancer therapy: a review, *Nanoscale Adv.*, 2021, **3**, 3332–3352.

43 A. Yuan, J. Wu, X. Tang, L. Zhao, F. Xu and Y. Hu, Application of Near-Infrared Dyes for Tumor Imaging, Photothermal, and Photodynamic Therapies, *J. Pharm. Sci.*, 2013, **102**, 6–28.

44 S. Chen, L. Zhu, Z. Du, R. Ma, T. Yan, G. Alimu, X. Zhang, N. Alifu and C. Ma, Polymer encapsulated clinical ICG nanoparticles for enhanced photothermal therapy and NIR fluorescence imaging in cervical cancer, *RSC Adv.*, 2021, **11**, 20850–20858.

45 M. Sevieri, F. Silva, A. Bonizzi, L. Sitia, M. Truffi, S. Mazzucchelli and F. Corsi, Indocyanine Green Nanoparticles: Are They Compelling for Cancer Treatment?, *Front. Chem.*, 2020, **8**, 550087.

46 Z. Sheng, D. Hu, M. Zheng, P. Zhao, H. Liu, D. Gao, P. Gong, G. Gao, P. Zhang, Y. Ma and L. Cai, Smart human serum albumin-indocyanine green nanoparticles generated by programmed assembly for dual-modal imaging-guided cancer synergistic phototherapy, *ACS Nano*, 2014, **8**, 12310–12322.

47 F. An, Z. Yang, M. Zheng, T. Mei, G. Deng, P. Guo, Y. Li and R. Sheng, Rationally assembled albumin/indocyanine green nanocomplex for enhanced tumor imaging to guide photothermal therapy, *J. Nanobiotechnol.*, 2020, **18**, 1–11.

48 H. Hu, J. Chen, H. Yang, X. Huang, H. Wu, Y. Wu, F. Li, Y. Yi, C. Xiao, Y. Li, Y. Tang, Z. Li, B. Zhang and X. Yang, Potentiating photodynamic therapy of ICG-loaded nanoparticles by depleting GSH with PEITC, *Nanoscale*, 2019, **11**, 6384–6393.

49 V. V. Zarubaev, T. C. Kris'ko, E. V. Kriukova and T. D. Muraviova, Effect of albumin on the fluorescence quantum yield of porphyrin -based agents for fluorescent diagnostics, *Photodiagn. Photodyn. Ther.*, 2017, **20**, 137–143.

50 H.-L. Shen, S. Cao, E. Ahokas, J. Cho, F. Nouizi, C.-S. Kim and G. Gulsen, Monitoring Distribution of the Therapeutic Agent Dimethyl Sulfoxide via Solvatochromic Shift of Albumin-Bound Indocyanine Green, *Sensors*, 2023, **23**, 7728.

51 T. S. Kondratenko, M. S. Smirnov, O. V. Ovchinnikov and I. G. Grevtseva, Luminescence of hybrid nanostructures based on colloidal Ag_2S/TGA quantum dots and Indocyanine Green molecules, *J. Nanopart. Res.*, 2020, **22**, 271.

52 V. Mundra, Y. Peng, S. Rana, A. Natarajan and R. I. Mahato, Micellar formulation of indocyanine green for phototherapy of melanoma, *J. Controlled Release*, 2015, **220**, 130–140.

53 R. Mačianskienė, M. Almanaitytė, R. Treinys, A. Navalinskas, R. Benetis and J. Jurevičius, Spectral characteristics of voltage-sensitive indocyanine green fluorescence in the heart, *Sci. Rep.*, 2017, **7**, 1–12.

54 R. Ma, N. Alifu, Z. Du, S. Chen, Y. Heng, J. Wang, L. Zhu, C. Ma and X. Zhang, Indocyanine green-based theranostic nanoplatform for nir fluorescence image-guided chemo/photothermal therapy of cervical cancer, *Int. J. Nanomed.*, 2021, **16**, 4847–4861.

55 M.-R. Wu, Y.-Y. Huang and J.-K. Hsiao, Use of Indocyanine Green (ICG), a Medical Near Infrared Dye, for Enhanced Fluorescent Imaging—Comparison of Organic Anion Transporting Polypeptide 1B3 (OATP1B3) and Sodium-Taurocholate Cotransporting Polypeptide (NTCP) Reporter Genes, *Molecules*, 2019, **24**, 2295.

56 H.-C. Tseng, C.-Y. Kuo, W.-T. Liao, T.-S. Chou and J.-K. Hsiao, Indocyanine green as a near-infrared theranostic agent for ferroptosis and apoptosis-based, photothermal, and photodynamic cancer therapy, *Front. Mol. Biosci.*, 2022, **9**, 1045885.

57 C. Zhang, T. Lu, J. Tao, G. Wan and H. Zhao, Co-delivery of paclitaxel and indocyanine green by PEGylated graphene oxide: a potential integrated nanoplatform for tumor theranostics, *RSC Adv.*, 2016, **6**, 15460–15468.

58 M. Kapałczyńska, T. Kolenda, W. Przybyła, M. Zajączkowska, A. Teresiak, V. Filas, M. Ibbs, R. Bliźniak, L. Luczewski and K. Lamperska, 2D and 3D cell cultures – a comparison of different types of cancer cell cultures, *Arch. Med. Sci.*, 2018, **14**, 910–919.

59 W. T. Lee, J. Yoon, S. S. Kim, H. Kim, N. T. Nguyen, X. T. Le, E. S. Lee, K. T. Oh, H.-G. Choi and Y. S. Youn, Combined Antitumor Therapy Using In Situ Injectable Hydrogels Formulated with Albumin Nanoparticles Containing Indocyanine Green, Chlorin e6, and Perfluorocarbon in Hypoxic Tumors, *Pharmaceutics*, 2022, **14**, 148.

60 G. Perini, E. Rosa, G. Friggeri, L. Di Pietro, M. Barba, O. Parolini, G. Ciasca, C. Moriconi, M. Papi, M. De Spirito and V. Palmieri, INSIDIA 2.0 High-Throughput Analysis of 3D Cancer Models: Multiparametric Quantification of Graphene Quantum Dots Photothermal Therapy for Glioblastoma and Pancreatic Cancer, *Int. J. Mol. Sci.*, 2022, **23**, 3217.